CHAPTER 5

From Nuclear Fluxes During Tunnelling to Electronic Fluxes During Charge Migration

DONGMING JIA,[a] JÖRN MANZ,*[a,b,c] AXEL SCHILD,[d] VÍT SVOBODA[d] AND YONGGANG YANG[a,c]

[a] State Key Laboratory of Quantum Optics and Quantum Optics Devices, Institute of Laser Spectroscopy, Shanxi University, 92 Wucheng Road, Taiyuan 030006, China; [b] Institut für Chemie und Biochemie, Freie Universität Berlin, Takustrasse 3, 14195 Berlin, Germany; [c] Collaborative Innovation Center of Extreme Optics, Shanxi University, 92 Wucheng Road, Taiyuan 030006, China; [d] Laboratorium für Physikalische Chemie, Eidgenössische Technische Hochschule, Vladimir-Prelog-Weg 2, 8093 Zürich, Switzerland
*Email: jmanz@chemie.fu-berlin.de

5.1 Introduction

The purpose of this chapter is to manifest a quantum dynamical analogy of intramolecular nuclear tunnelling and electronic charge migration, with special emphasis on the corresponding nuclear and electronic fluxes. On first glance, the two processes may appear so different that one may not expect any analogy between them: on the one hand, nuclear tunnelling is a reactive process that transforms a ''reactant'' isomer into a ''product'' isomer by means of large-amplitude motions of the nuclei, in typical time domains of picoseconds (ps) or even much longer. Reactants and products are centred

Theoretical and Computational Chemistry Series No. 18
Tunnelling in Molecules: Nuclear Quantum Effects from Bio to Physical Chemistry
Edited by Johannes Kästner and Sebastian Kozuch

Published by the Royal Society of Chemistry, www.rsc.org

at two different minima of the potential energy surface (PES) of the molecular system in its electronic ground state, and they are separated from each other by the barrier of the PES. The system's energy is below the barrier, which means the reaction from the reactant to the product is classically forbidden – it proceeds by quantum mechanical tunnelling through the barrier. On the other hand, electronic charge migration is a non-reactive process at much higher energies that involves not just the electronic ground state. This allows the electronic charge to flow from one molecular site to another, in typical time domains from few hundred attoseconds (as) to few femtoseconds (fs); by comparison, nuclear motions appear to be nearly frozen in this time domain.

The quantum dynamics of nuclear tunnelling has been investigated from the early days of quantum mechanics[1] up to today; for an outstanding example of the present state-of-the-art, see the work by Fábri *et al.* on tunnelling isomerization of ammonia and its isotopomers, including stereomutation of NHDT;[2] see also the complementary chapters of this book.[3] For comparison, the first presentation of the quantum dynamics of charge migration is in the 1944 textbook on quantum chemistry by Eyring *et al.*;[4] however, this was largely forgotten[5] so the first experimental signatures of the process[6] came as a rediscovery that launched the renaissance of the field, see for example ref. 7–12 and the surveys of the literature in ref. 13 and 14. A prominent example is the first joint experimental and theoretical reconstruction of charge migration in the iodoacetylenic cation $HCCI^+$.[14,15] We call special attention to the two recent papers by Fábri *et al.* on tunnelling of NH_3 and NHDT,[2] and by Kraus *et al.* on charge migration in $HCCI^+$,[15] because they serve as important references for the subsequent quantum dynamics simulations of similar processes in similar model systems, the stereomutation of the CHFBr radical by nuclear tunnelling, and electronic charge migration in the bromoacetylenic cation $HCCBr^+$. The results will be used to illustrate the analogy of nuclear tunnelling and electronic charge migration.

The general quantum theory for the analogous processes, nuclear tunnelling and electronic charge migration, will be presented in Section 5.2, with special focus on the nuclear and electronic fluxes, *cf.* ref. 16. In order to emphasize the analogy, Section 5.2 uses common notations for both processes. Illuminating applications with more special notations for the two examples are given in Sections 5.3 and 5.4. Specifically, for the case of nuclear tunnelling, we consider the umbrella inversion of the CHFBr radical, as illustrated by the cartoon in Figure 5.1. Important properties of the system have been discovered and analysed recently; see the joint experimental and theoretical ref. 17 and 18. Section 5.3 presents the results that are essential for the present purpose. Section 5.4 presents analogous new results for the case of charge migration in $HCCBr^+$, as illustrated by the cartoon in Figure 5.2. The analogy of the results for nuclear tunnelling of CHFBr (Section 5.3) and for charge migration in $HCCBr^+$ of (Section 5.4) is discussed in Section 5.5. The conclusions are given in Section 5.6.

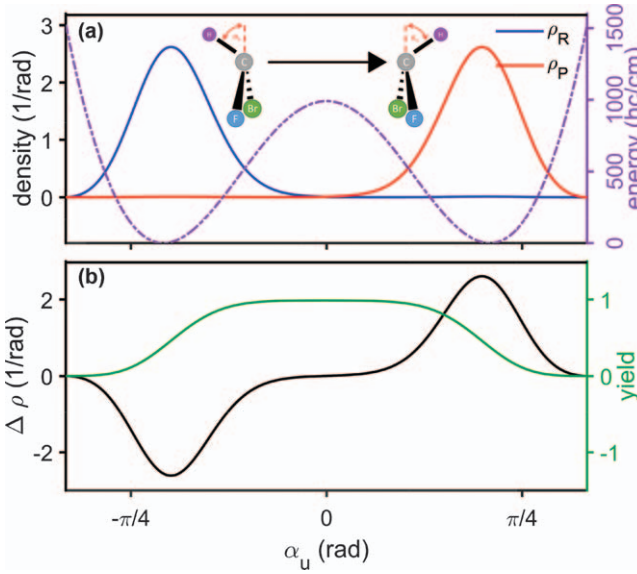

Figure 5.1 Periodic stereomutation of the CHFBr radical by nuclear tunnelling, from the reactant S-enantiomer (left) to the product R-enantiomer (right) along the angle α_u for umbrella inversion, and back. (a) Illustration of the stereomutation. The symmetric double-well potential energy curve $V(\alpha_u)$ with two equivalent minima which support the two enantiomers is shown as purple dashed line. The horizontal line is at the mean energy of the two vibrational levels E_g and E_e for the ground and excited states of the lowest tunnelling doublet – they coincide within graphical resolution. The level splitting is $\Delta E = E_e - E_g = 3.16$ h c cm^{-1}; the corresponding tunnelling period is $\tau_{stereo} = h/\Delta E = 10.57$ ps. The horizontal line serves as baseline for the densities $\rho_R(\alpha_u)$ and $\rho_P(\alpha_u)$ of the reactant (R, blue) and product (P, red). The horizontal arrow symbolizes the nuclear flux from R to P during the first half period, $0 \le t \le \tau_{stereo}/2$. (b) Density difference $\Delta\rho(\alpha_u) = \rho_P(\alpha_u) - \rho_R(\alpha_u)$ (black) and the resulting yield $y(\alpha_u)$ (green). The yield serves as spatial profile of the flux, *cf.* eqn (5.28) and (5.29) and Figure 5.3(c).

5.2 Quantum Theory

In order to establish the analogy of nuclear tunnelling and electronic charge migration, we employ simple models. Examples will be presented in Sections 5.3 and 5.4, respectively. Refinements and extensions will be discussed in the conclusions in Section 5.6. To begin with, we employ two-state models, with two vibrational states for applications to nuclear tunnelling, and with two electronic states for electronic charge migration. For convenience, we consider the scenarios where one of the two states is the ground (g) state and the other one is the next vibrationally or electronically excited (e) state. The two states are represented by the corresponding quantum mechanical wave functions Ψ_g and Ψ_e with energies E_g and E_e. To emphasize the analogy, we employ the same notations for the two different phenomena, which means in the cases of nuclear tunnelling and electronic charge migration, Ψ_g, Ψ_e and

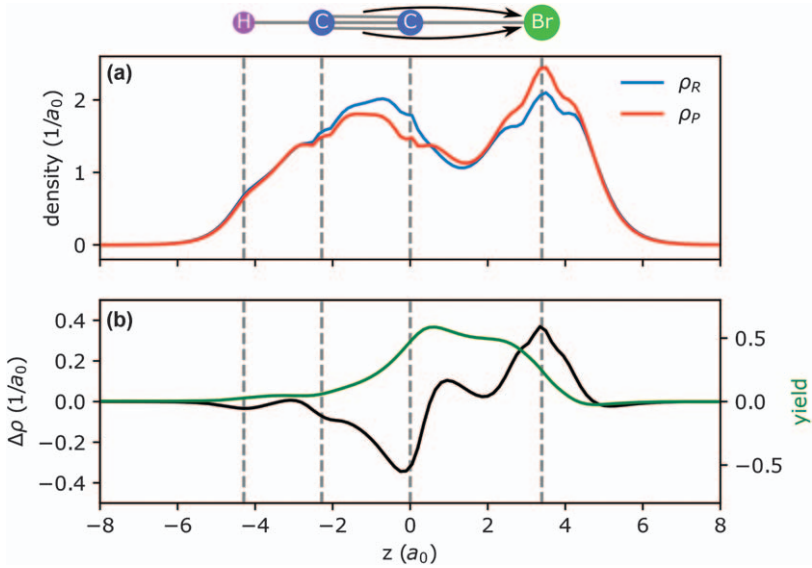

Figure 5.2 Periodic electronic charge migration in the linear $HCCBr^+$ cation along its axis z. (a) Cartoon of $HCCBr^+$ with the nuclei fixed at the global minimum structure of the precursor molecule HCCBr in the electronic ground state ($\tilde{X}^+\,^1\Sigma^+$). Initially, the cation is prepared in the reactant (R) superposition state $1/\sqrt{2}(\Psi_g + \Psi_e)$ of the electronic ground state Ψ_g ($g = \tilde{X}^+\,^2\Pi$) and the first-excited state Ψ_e ($e = \tilde{A}^+\,^2\Pi$). The corresponding electronic eigenenergies are E_g and E_e, with energy gap $\Delta E = E_e - E_g = 2.74$ eV. The reactant (R) state evolves periodically to the product (P) superposition state, which is represented by $1/\sqrt{2}\,(\Psi_g - \Psi_e)$ (except for an irrelevant phase factor), and then back to R. The period for one cycle $R \rightarrow P \rightarrow R$ is $\tau_{chm} = h/\Delta E = 1.51$ fs. Also shown are the one-dimensional axial densities of the valence electrons $\rho_R(z)$ (blue) of the initial state ("reactant" R) and $\rho_P(z)$ (red) for the corresponding "product" (P) state; they are obtained by integrating the related 3D one-electron densities of the valence electrons over the planes (x, y) perpendicular to the molecular axis (z). The curved, nearly horizontal arrows symbolize the flux of the valence electrons during the first half period $0 \le t \le \tau_{chm}/2$, mainly from the acetylenic moiety to the domain close to the bromine nucleus. (b) The density difference $\Delta\rho(z) = \rho_P(z) - \rho_R(z)$ (black) and the resulting yield $y(z)$ (green). The yield serves as spatial profile of the electronic flux that is shown in Figure 5.4(c), *cf.* eqn (5.28) and (5.29).

E_g, E_e represent nuclear and electronic wave functions and energies, respectively. The wave functions depend on the specific coordinates of the molecule (or the molecular radical or ion, or in general the molecular "model system"). For the time being, these coordinates will not be written down explicitly. For simplicity, we consider scenarios of oriented model systems.

The wave functions Ψ_g, Ψ_e and energies E_g, E_e are evaluated as eigenfunctions and eigenenergies of the time-independent Schrödinger equation (TISE)

$$H\,\Psi_j = E_j\,\Psi_j,\; j = g,\, e \tag{5.1}$$

where H denotes the system's model Hamiltonian. In the case of tunnelling, the two states belong to the lowest tunnelling doublet of the molecular system in its electronic ground state, embedded in a symmetric double-well potential. Effects of nuclear and electronic couplings are assumed to be negligible, *i.e.* the nuclear wave functions and energies Ψ_g, Ψ_e and E_g, E_e may be evaluated in the frame of the Born–Oppenheimer approximation (BOA).[19,20] Likewise, in the case of charge migration, the electronic wave functions and energies Ψ_g, Ψ_e and E_g, E_e of the system are evaluated using the approximation of fixed nuclei, *i.e.* again in the frame of the BOA, without consideration of the couplings between electrons and the nuclei. The effects of the couplings will also be discussed in the conclusions.

For special cases, the wave functions Ψ_g, Ψ_e are real-valued, but in general they are complex,

$$\Psi_j = \psi_j \exp(i\ \delta_j), j = \mathrm{g},\ \mathrm{e}, \tag{5.2}$$

with real-valued functions ψ_j and phases δ_j that depend on the coordinates.

We consider the scenario where the initial state of the system is prepared as superposition state

$$\Psi(t=0) = C_g\ \Psi_g + C_e\ \Psi_e. \tag{5.3}$$

The coefficients C_g and C_e may be real, and they may be equal to each other (*e.g.* $C_g = C_e = 1/\sqrt{2}$), but in general they are complex and not equal to each other,

$$C_j = c_j \exp(i\ \eta_j), j = \mathrm{g},\ \mathrm{e} \tag{5.4}$$

with real-valued amplitudes $c_j \geq 0$ and phases η_j. The corresponding initial populations (or occupation probabilities) of the ground and excited states,

$$P_g(t=0) = {c_g}^2,\ P_e(t=0) = {c_e}^2 \tag{5.5}$$

are normalized,

$$P_g(t=0) + P_e(t=0) = {c_g}^2 + {c_e}^2 = 1. \tag{5.6}$$

The system's time evolution is described in terms of the time dependent wave function $\Psi(t)$. It is evaluated as solution of the time-dependent Schrödinger equation (TDSE)

$$i\ \hbar\ \mathrm{d}/\mathrm{d}t\ \Psi(t) = H\ \Psi(t) \tag{5.7}$$

with initial value (5.3). The result is

$$\Psi(t) = C_g \exp(-i\ E_g\ t/\hbar)\ \Psi_g + C_e \exp(-i\ E_e\ t/\hbar)\ \Psi_e. \tag{5.8}$$

The corresponding populations of states g and e are time independent,

$$P_g(t) = P_g(t=0) = {c_g}^2,\ P_e(t) = P_e(t=0) = {c_e}^2. \tag{5.9}$$

This means that, for our scenarios, there are no transitions that transfer the population between states g and e – the system evolves adiabatically.

The time evolution of the system's density is

$$\sigma(t) = |\Psi(t)|^2 = P_g\ \sigma_g + P_e\ \sigma_e + 2\ c_g\ c_e\ \psi_g\ \psi_e \cos\left(\Delta E\ t/\hbar - \Delta\delta - \Delta\eta\right). \tag{5.10}$$

Here

$$\sigma_g = {\psi_g}^2,\ \sigma_e = {\psi_e}^2 \tag{5.11}$$

denote the time-independent densities of the ground and excited states,

$$\Delta E = E_e - E_g \tag{5.12}$$

is the energy gap between the states, and

$$\Delta\delta = \delta_e - \delta_g,\ \Delta\eta = \eta_e - \eta_g \tag{5.13}$$

are the phase differences. Apparently, the density evolves periodically, with period[1]

$$\tau = h/\Delta E \tag{5.14}$$

where h denotes Planck's constant.

In the applications below, we consider the scenarios where the eigenfunctions are real-valued, such that $\Delta\delta = 0$ in eqn (5.10) and (5.13). Moreover, the results do not depend on the absolute phase of the wave function $\Psi(t)$, which means we may set $\eta_g = 0$ and $\Delta\eta = \eta_e$ in eqn (5.4), (5.10) and (5.13). Eqn (5.10) then simplifies to

$$\sigma(t) = |\Psi(t)|^2 = P_g\ \sigma_g + P_e\ \sigma_e + 2\ c_g\ c_e\ \Psi_g\ \Psi_e \cos\left(\Delta E\ t/\hbar - \Delta\eta\right). \tag{5.15}$$

For the present purposes, it is convenient to rewrite eqn (5.15) in the way laid out in ref. 21, with proper adaption of the notation. Accordingly, we employ the variable

$$t' = t - t_{\Delta\eta} \tag{5.16}$$

which denotes the time shifted by

$$t_{\Delta\eta} = \Delta\eta\ \hbar/\Delta E = \tau\ \Delta\eta/2\pi. \tag{5.17}$$

The densities at times $t' = 0$ and $t' = \tau/2$ when the cos term in eqn (5.15) achieves its maximum and minimum values are labelled by R (''reactant'') and P (''product''),

$$\sigma_R = P_g\ \sigma_g + P_e\ \sigma_e + 2\ c_g\ c_e\ \Psi_g\ \Psi_e \tag{5.18}$$

$$\sigma_P = P_g\ \sigma_g + P_e\ \sigma_e - 2\ c_g\ c_e\ \Psi_g\ \Psi_e, \tag{5.19}$$

respectively. Let us take a minute here to discuss the definitions of the ''reactant'' and ''product'' in eqn (5.18) and (5.19). From a formalistic point of view, the assignments of the right-hand sides of eqn (5.18) and (5.19) to ''R'' and ''P'' are arbitrary, because the signs of the real-valued wave functions Ψ_g and Ψ_e are arbitrary – both Ψ_g, Ψ_e and $-\Psi_g$, $-\Psi_e$ are solutions of

the TISE [eqn (5.1)]. By convention, the sign of the wave function of the ground state is set such that Ψ_g is dominantly positive, but for Ψ_e, there is no such rule. That means that we are free to determine the sign of Ψ_e such that the assignment of "R" in eqn (5.18) conforms to the experimental preparation of the "reactant". The definition of the "product" in eqn (5.19) then follows automatically. Applications will be demonstrated in Sections 5.3 and 5.4.

Using the density difference

$$\Delta\sigma = \sigma_P - \sigma_R = -4\ c_g\ c_e\ \Psi_g\ \Psi_e \tag{5.20}$$

the time evolution of the density (5.15) can be rewritten in compact form,

$$\sigma(t) = \sigma_R + \Delta\sigma\ \sin^2(\pi t'/\tau). \tag{5.21}$$

The first term in eqn (5.21) is the (time-independent) density of the reactant, which serves as a reference. The second term accounts for the deviation of the density at time t from the reference. The periodicity of the $\sin^2$-function implies that the density alternates between $\sigma(t) = \sigma_R$ for $t = 0,\ \tau,\ 2\tau,\ \ldots$ and $\sigma(t) = \sigma_P$ for $t = \tau/2,\ 3\tau/2,\ 5\tau/2, \ldots$. Furthermore, eqn (5.20) and (5.21) show that efficient periodic shifts of the density from the reactant to the product and back call for good overlap of the wave functions Ψ_g and Ψ_e, or turning the table, there is neither tunnelling nor charge migration if Ψ_g and Ψ_e do not overlap. Eqn (5.20) and (5.21) also tell us that for the given wave functions Ψ_g and Ψ_e of the ground and excited states, the most efficient shift of the density is obtained if the product of the coefficients achieves its maximum value

$$\max\ c_g\ c_e = \tfrac{1}{2} \text{ for } c_g = c_e = 1/\sqrt{2}, \tag{5.22}$$

cf. eqn (5.6). That means, in the ideal case, the superposition state (5.3) should be prepared with equal populations of the ground and excited states, $P_g = P_e = \frac{1}{2}$.[21]

In principle, the wave functions Ψ_g, Ψ_e and the densities $\sigma(t)$, σ_g, σ_e and $\Delta\sigma$ in eqn (5.15) and (5.21) depend on all coordinates of the system. It is helpful to reduce these high-dimensional (high-D) densities to low-D ones, for example to 3D or even to 1D ones. In the subsequent applications to nuclear tunnelling and to electronic charge migration, we shall employ 1D densities which depend on the corresponding nuclear or electronic coordinate q, respectively. The 1D densities will be denoted by the letter "ρ", in order to distinguish them from the high-D densities that are denoted by "σ". Thus eqn (5.21) is reduced to

$$\rho(q,\ t) = \rho_R(q) + \Delta\rho(q)\ \sin^2(\pi\ t'/\tau). \tag{5.23}$$

Various methods for reducing high-D to 1D densities are detailed in ref. 16. Two examples will be demonstrated in Sections 5.3 and 5.4.

Next, we determine the nuclear or electronic fluxes $F(q, t)$ during tunnelling and charge migration, respectively. Fluxes and densities are complementary to each other, which means at a given time t, the density $\rho(q, t)$ of the system

tells us where it is, whereas the flux $F(q, t)$ quantifies its temporal rate and direction of change. In 3D models, the flux $F(q, t)$ at time t determines the number of particles that flow through a surface perpendicular to the coordinate q per time, at the instant t. Positive and negative values of $F(q, t)$ mean that the particles flow along q, or in the opposite direction, respectively.

In 1D models, the fluxes $F(q, t)$ are equal to the 1D flux densities $j(q, t)$.[16] They are related to the corresponding densities $\rho(q, t)$ by means of the 1D continuity equation,

$$\partial\rho(q, t)/\partial t + \partial j(q, t)/\partial q = 0 \tag{5.24}$$

with boundary conditions that depend on the system.[16] In the present applications, we consider scenarios where both the density as well as the flux are negligible for values of q smaller than some minimum value, $q_{\min}$,

$$\rho(q, t) = 0,\ F(q, t) = j(q, t) = 0 \text{ for } q \leq q_{\min}. \tag{5.25}$$

The 1D flux can then be evaluated by integration of the continuity eqn (5.24), with the boundary conditions (5.25). The result is

$$F(q,t) = j(q,t) = -\int_{q_{\min}}^{q} \mathrm{d}q'\ \partial\rho(q',t)/\partial t. \tag{5.26}$$

We re-emphasize that the densities and flux (densities) carry complementary information about the system. For example, in applications where one has complete knowledge about the time evolution of the density $\rho(q, t)$, this still does not suffice to calculate the flux $F(q, t)$ or the flux density $j(q, t)$, because one also needs boundary conditions such as in eqn (5.25).[22] Turning the tables, two identical or practically indistinguishable densities $\rho(q, t)$ may be associated with two entirely different fluxes or flux densities, depending on the boundary conditions.[23]

For the present 1D two-state models with time evolutions of the density specified by eqn (5.23), the time derivative in eqn (5.26) can be carried out analytically. As a result, the boundary condition (5.25) yields the 1D flux or flux density

$$F(q,t) = j(q,t) = -\int_{q_{\min}}^{q} \mathrm{d}q' \Delta\rho(q')\pi/\tau \sin(2\pi t'/\tau). \tag{5.27}$$

Accordingly, the flux depends exclusively on the time-dependent part of the density, eqn (5.15) or (5.23). It evolves periodically, with the same period τ as the density, eqn (5.14), but with phase shift $\pi/2$. As a consequence, maximum or minimum shifts of the density at the times when $\cos(2\pi t'/\tau) = \pm 1$ correlate with zero fluxes, and *vice versa.*

Finally, it is instructive to consider the yield $y(q)$ of the flux,[13,24] which means the time integrated number of particles that pass *via* q when they flow

from the domain $q_{\min} \leq q' \leq q$ to the complementary domain $q \leq q'$ during the half period $0 \leq t' \leq \tau/2$,

$$y(q) = \int_0^{\tau/2} \mathrm{d}t' j(q, t') = -\int_{q_{\min}}^{q} \mathrm{d}q' \Delta\rho(q'). \tag{5.28}$$

The 1D flux or flux density (5.27) can, therefore, also be expressed as

$$F(q, t) = j(q, t) = y(q)\ \pi/\tau\ \sin\ (2\pi t'/\tau). \tag{5.29}$$

Eqn (5.29) tells us that the 1D flux or the 1D flux density evolves with robust spatial profile $y(q)$, and this is modulated by the periodic time evolution factor, $\sin\ (2\pi t'/\tau)$. Alternating maximum and minimum values of the fluxes in forward and backward directions from R to P and from P to R are achieved at times $t' = \tau/4,\ 5\tau/4,\ 9\tau/4, \ldots$ and $t' = 3\tau/4,\ 7\tau/4,\ 11\tau/4, \ldots$, respectively. The maximum absolute values of the fluxes are reciprocal to the period τ, or they are proportional to the energy gap ΔE between the levels of the excited and ground states, *cf.* eqn (5.14).

5.3 Application to the Stereomutation of CHFBr by Nuclear Tunnelling

Our first application of the general quantum theory for the analogy of nuclear tunnelling and electronic charge migration is to the stereomutation of the CHFBr radical; as an example of nuclear tunnelling, see Figure 5.1. There are several motivations for the choice of this system:

Experimentally, the stereomutation of CHFBr is initiated by enantiomer selective preparation of the precursor (*S*)-CHFBrI, and by photo-dissociating it according to the scheme[17,18]

$$\begin{aligned}(S)\text{-CHFBrI} \rightarrow (S)\text{-CHFBrI}^* \rightarrow (S)\text{-CHFBr} - \text{I} \rightarrow (R)\text{-CHFBr} - \text{I} \\ \rightarrow (S)\text{-CHFBr} + \text{I} \rightarrow (R)\text{-CHFBr} + \text{I} \rightarrow (S)\text{-CHFBr} + \text{I} \rightarrow \ldots.\end{aligned} \tag{5.30}$$

Specifically, an ultrashort UV laser pump-pulse (wavelength 266 nm, full temporal width at half maximum, FWHM = 70 fs) excites the educt (*S*)-CHFBrI from its electronic ground state $\tilde{X}^{+1}$A to the dissociative state $\tilde{A}^{+}\ ^{1}$E(1). This induces two processes, namely C–I bond breaking as well as stereomutation from the (*S*)-enantiomer to the (*R*)-enantiomer, and back. The two processes are launched simultaneously, which means the first cycle of stereomutation starts during photodissociation. After photodissociation, the stereomutation persists in the CHFBr radical. Experimental details are presented in ref. 17 and 18. Suffice it here to say that the bond breaking is measured by means of time-resolved photo-ion yield spectroscopy (TR-PIS) as well as photo-electron pump (266 nm)–probe (133 nm) spectroscopy (TR-PES). The stereomutation is monitored by means of a new technique: time-resolved photoelectron circular dichroism (TR-PECD). Accordingly, the photodissociation is completed after about 70 fs, whereas the first cycle of stereomutation ("(*S*)-CHFBr − I → (*R*)-CHFBr − I → (*S*)-CHFBr + I" in

eqn (5.30)) takes about 200 fs; subsequently, it slows down to the ps time domain. The experimental TR-PECD spectra suggest stereomutation of the CHFBr radical by tunnelling,

$$(S)\text{-CHFBr} \rightarrow (R)\text{-CHFBr} \rightarrow (S)\text{-CHFBr} \rightarrow \ldots \tag{5.31}$$

[compare with the second line of eqn (5.30)], with tunnelling period $\tau_{\text{stereo}} \approx 10$ ps, for a full cycle from R to P and back to R. The results presented in ref. 17 and 18 provide the first experimental observation of stereomutation in the fs-to-ps time domain. This attracts our attention to the model system, calling for its quantum dynamics simulation.

The present investigation of the stereomutation of CHFBr by tunnelling, eqn (5.31), is encouraged furthermore by recent quantum dynamical simulations of the analogous stereomutation of the isotopically substituted ammonia molecule[2]

$$(S)\text{-NHDT} \rightarrow (R)\text{-NHDT} \rightarrow (S)\text{-NHDT} \rightarrow \ldots. \tag{5.32}$$

Here the representative nuclear wave function was propagated in full dimensionality (full-D) on the PES of ammonia in the electronic ground state, without considerations of any couplings to more excited states. The PES was evaluated by means of quantum chemistry state-of-the-art *ab initio* methods. Similar quantum dynamics simulations were also performed for the umbrella inversion of the non-substituted ammonia by tunnelling.[2] The results for the full-D nuclear fluxes of $^{14}NH_3$ were then compared with our previous quantum dynamical results based on a two-state model[25] with empirical 1D model potential.[26] The full-D and 1D results agree with each other almost quantitatively.[2] This supports the present 1D quantum dynamical two-state model simulation of the stereomutation (5.31) by nuclear tunnelling.

Thus, we perform a quantum dynamics model simulation of the stereomutation of the CHFBr radical (5.31). Specifically, we employ a 1D model for the nuclear tunnelling along the angle α_u for the umbrella (u) inversion of CHFBr, as illustrated in Figure 5.1(a). The angle α_u thus takes the role of the generic coordinate which is called "q" in Section 5.2. The corresponding 1D model Hamiltonian is

$$H(\alpha_u) = -\hbar^2\, \partial^2/2\, I\, \partial\, {\alpha_u}^2 + V(\alpha_u). \tag{5.33}$$

The first term accounts for the kinetic energy of the angular nuclear motion along α_u, with moment of inertia $I = m_H\, {R_{CH}}^2$, where $m_H = 1.0079$u is the mass of the hydrogen atom, and R_{CH} is the C–H bond length which is approximately constant during the umbrella inversion, $R_{CH} = 1.08$ Å. This expression for the kinetic energy is equivalent to the term used in ref. 25. The details of the construction of this kinetic energy operator, by reduction of the full-D expression to the 1D model, are presented in ref. 18, based on the general approach of ref. 27 to applications in terms of arbitrary curvilinear coordinates.

The second term in eqn (5.33) is the potential energy curve along α_u, illustrated in Figure 5.1(a). It is a symmetric double-well potential. The "left"

and "right" potential wells support the reactant (R) and product (P) enantiomers, which are centred at the potential minima at $\alpha_{uR} = -38^\circ$ and at $\alpha_{uP} = -\alpha_{uR} = +0.66$ rad $(+38^\circ)$, respectively. For convenience, we define corresponding domains of R ($\alpha_u < 0$) and P ($\alpha_u > 0$). These domains are separated from each other by the potential barrier at $\alpha_u = \alpha_{ub} = 0$, also called the transition state, $\ddagger$. The corresponding cartoons of R and P in Figure 5.1(a) are mirror images of each other, with the mirror plane in vertical orientation perpendicular to the paper plane. The potential curve $V(\alpha_u)$ has been calculated by means of the ORCA program package,[28] by performing a relaxed scan at the Møller–Plesset-2 level of quantum chemistry, with the correlation consistent valence basis set from the Karlsruhe basis set family, specifically valence triple-zeta and two sets of polarization functions and a set of diffuse functions def2-TZVPPD for use with the Stuttgart–Dresden–Bonn relativistic effective core potentials on all atoms,[29] see ref. 18 for the details.

The TISE (5.1) with model Hamiltonian (5.33) is solved for the two real-valued eigenfunctions Ψ_g and Ψ_e and for the energies E_g and E_e of the ground and first excited vibrational states by means of the discrete variable representation (DVR) method[30] on a fine, regularly spaced grid in the angular range $-\pi/3$ rad $\leq \alpha_u \leq +\pi/3$ rad $(-60^\circ \leq \alpha_u \leq +60^\circ)$. The resulting energies and the tunnelling splitting $\Delta E = E_e - E_g = 3.16$ h c cm^{-1} are illustrated in Figure 5.1(a). The corresponding time for one cycle R → P → R of the stereomutation (5.33) is $\tau_{stereo} = h/\Delta E = 10.57$ ps. The general notation "τ" of Section 5.2 is thus specified as "τ_{stereo}", for the present application to stereomutation of CHFBr. (Note that the value 5.285 ps that is given in ref. (18) applies to the half cycles R → P and P → R.) The symmetry of the double-well potential $V(\alpha_u)$ implies that $\Psi_g(\alpha_u) = \Psi_g(-\alpha_u)$ and $\Psi_e(\alpha_u) = -\Psi_e(-\alpha_u)$ are symmetric and antisymmetric with respect to the umbrella inversion angle α_u, respectively; these symmetry relations for the wave functions impose various symmetry properties on the nuclear densities and the nuclear fluxes and these are specified below. The signs of the wave functions are chosen such that they are consistent with the experimental preparation of the reactant enantiomer [=(*S*)-CHFBr], see the discussion after eqn (5.18) and (5.19). Specifically, we set $\Psi_g(\alpha_u) > 0$, in accord with the standard convention, and $\Psi_e(\alpha_u)$ is positive in the domain of the reactants ($\alpha_u < 0$) but negative in the domain of the products ($\alpha_u > 0$).

The resulting nuclear angular densities $\rho_R(\alpha_u)$ and $\rho_P(\alpha_u)$ of the reactant (R, red) and product (P, blue) embedded in the left and right wells of $V(\alpha_u)$ are also illustrated in Figure 5.1(a). For symmetry reasons, $\rho_P(\alpha_u) = \rho_R(-\alpha_u)$. Both $\rho_R(\alpha_u)$ and $\rho_P(\alpha_u)$ have single maxima that are located close to the left and right minima of the double minimum potential at α_{uR} and α_{uP}, respectively. The values of $\rho_R(\alpha_u)$ and $\rho_P(\alpha_u)$ at $\alpha_u = 0$, *i.e.* at the barrier of the potential curve, are negligible.

Figure 5.1(b) has the nuclear density difference $\Delta\rho(\alpha_u) = \rho_P(\alpha_u) - \rho_R(\alpha_u)$ (black) and the nuclear yield $y(\alpha_u)$ (green), *cf.* eqn (5.20) and (5.28). For symmetry reasons, $\Delta\rho(\alpha_u) = -\Delta\rho(-\alpha_u)$, $\Delta\rho(\alpha_u = 0) = 0$ and $y(\alpha_u) = y(-\alpha_u)$. The value of $\Delta\rho(\alpha_u)$ is negative in the reactant domain but positive in the product domain. The yield is always positive. A significant property of the

yield $y(\alpha_u)$ – with important consequences for the nuclear fluxes $F(\alpha_u, t)$ – is that it has a plateau in the domain of the potential barrier, with maximum value at the top of the barrier ($\alpha_u = 0$).

In accord with the experimental initiation of the stereomutation of the CHFBr radical,[17,18] and also for convenience, we set the time $t = 0$ when the nuclear tunnelling starts from the reactant (*S*)-enantiomer. This means that the initial superposition of the wave function (5.3) is prepared with equal coefficients, $C_g = C_e = 1/\sqrt{2}$, and the phases in eqn (5.4) are equal to zero. This scenario simplifies the application of the general theory of Section 5.2. In particular, the time shift in eqn (5.17) is equal to zero, such that $t' = t$ in all subsequent equations for the densities and for the fluxes or the 1D flux densities.

The resulting time evolution of the nuclear angular density $\rho(\alpha_u, t)$ during the first cycle ($0 \le t \le \tau_{stereo} = 10.57$ ps) of the periodic stereomutation (5.31) of CHFBr by umbrella inversion is illustrated in Figure 5.3(a). For symmetry reasons, $\rho(\alpha_u, t) = \rho(-\alpha_u, \tau_{stereo}/2 - t) = \rho(-\alpha_u, \tau_{stereo}/2 + t) = \rho(\alpha_u, \tau_{stereo} - t)$. This implies the special symmetry relation $\rho(\alpha_u, \tau_{stereo}/4) = \rho(-\alpha_u, \tau_{stereo}/4) = \rho(\alpha_u, 3\tau_{stereo}/4) = \rho(-\alpha_u, 3\tau_{stereo}/4)$. Accordingly, the initial density of the reactant ($t = 0$) tunnels to the product ($t = \tau_{stereo}/2$) and then back to the reactant ($t = \tau_{stereo}$). At the intermediate times $t = \tau_{stereo}/4$ and $t = 3\tau_{stereo}/4$, the total nuclear density is separated into two equivalent parts for the reactant and for the product. Thus, during the first half period ($0 \le t \le \tau_{stereo}/2$), the nuclear density grows for the product at the expense of the reactant, without any significant appearance at the potential barrier, and *vice versa* during the second half period ($\tau_{stereo}/2 \le t \le \tau_{stereo}$).

Figure 5.3(b) illustrates the corresponding changes of the nuclear angular density $\rho(\alpha_u, t)$ compared to the initial density $\rho(\alpha_u, t = 0) = \rho_R(\alpha_u)$. For symmetry reasons, $\Delta\rho(\alpha_u, t) = \rho(\alpha_u, t) - \rho_R(\alpha_u) = -\Delta\rho(-\alpha_u, t) = \Delta\rho(\alpha_u, \tau_{stereo} - t) = -\Delta\rho(-\alpha_u, \tau_{stereo} - t)$, and the transfer of nuclear density from R to P and back to R implies that $\Delta\rho(\alpha_u, t) < 0$ in the reactant domain ($\alpha_u < 0$), in contrast with $\Delta\rho(\alpha_u, t) > 0$ in the product domain ($\alpha_u > 0$).

Finally, the periodic nuclear flux $F(\alpha_u, t)$ [or the equivalent 1D flux density $j(\alpha_u, t)$] along the umbrella inversion angle α_u during the first cycle ($0 \le t \le \tau_{stereo} = 10.57$ ps) is shown in Figure 5.3(c). In accord with eqn (5.29), the angular profile of the flux is equal to the yield $y(\alpha_u)$, and this is modulated by the sinusoidal time evolution with period τ_{stereo}. As a consequence, the nuclear angular flux has the symmetry relations $F(\alpha_u, t) = F(-\alpha_u, t)$ and $F(\alpha_u, t) = F(\alpha_u, \tau_{stereo}/2 - t) = -F(\alpha_u, \tau_{stereo}/2 + t) = -F(\alpha_u, \tau_{stereo} - t)$. Apparently, the nuclear angular flux $F(\alpha_u, t)$ is positive during the first half cycle ($0 < t < \tau_{stereo}/2$) when R tunnels along α_u to P, whereas it is negative during the second half cycle ($\tau_{stereo}/2 < t < \tau_{stereo}$) when P tunnels back to R. At the switches of the directions, $F(\alpha_u, t) = 0$ for $t = 0$, $\tau_{stereo}/2$, τ_{stereo}, $3\tau_{stereo}/2$, *etc.* In contrast, the "local" maximum and minimum values of the flux $F(\alpha_u, t)$ at umbrella inversion angle α_u are obtained at $t = \tau_{stereo}/4$, $5\tau_{stereo}/4$, $9\tau_{stereo}/4$,... and at $3\tau_{stereo}/4$, $7\tau_{stereo}/4$, $11\tau_{stereo}/4$,..., respectively.

Quite remarkable is the fact that the "global" maxima of the "forward" flux from R to P, and the minima of the "backward" flux from P to R, occur at

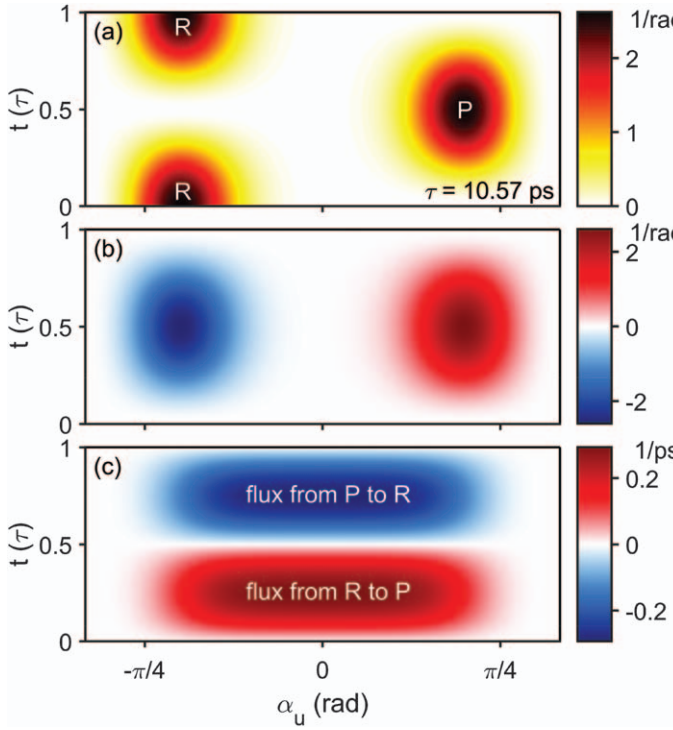

Figure 5.3 Time evolution of the periodic stereomutation of the CHFBr radical by nuclear tunnelling, from the reactant (*R*) *S*-enantiomer to the product (P) *R*-enantiomer along the angle α_u for umbrella inversion, and back, during the first period, $0 \leq t \leq \tau_{stereo} = 10.57$ ps; compare with Figure 5.1. (a) Nuclear density $\rho(\alpha_u, t)$. The value 0.008 rad^{-1} of $\rho(\alpha_u, t)$ at the planar configuration ($\alpha_u = 0$) is very small compared to the maximum values 2.622 rad^{-1} close to the potential minima. (b) Difference in the nuclear density $\rho(\alpha_u, t)$ at time t minus the initial density of the reactant, $\rho(\alpha_u, 0) = \rho_R(\alpha_u)$. (c) One-dimensional (1D) nuclear flux $F(\alpha_u, t)$, from R to P and back. At $t = \tau_{stereo}/2$, the flux changes sign, hence $F(\alpha_u, t = \tau_{stereo}/2) = 0$. The 1D flux is equal to the 1D nuclear flux density $j(\alpha_u, t)$. The results (a)–(c) are illustrated by color-coded contour plots.

$\alpha_u = 0$, *i.e.* at the potential barrier where the nuclear density is always exceedingly small. Moreover, in the entire domain of the barrier, the values of the flux are just slightly below (above) those maximum (minimum) values – the angular shape of the flux, *i.e.* the yield, has a plateau in the domain of the potential barrier, *cf.* Figure 5.1(b). This result, which may appear paradoxical at first glance, can be rationalized by the following interpretation:[31] the nuclei of the CHFBr radical prefer the two equivalent global minimum structures, either R or P, and they try to avoid the structure of the "transition state" (⧺) at the potential barrier. However, the radical is prepared initially in the superposition state (5.3) – this is not in an eigenstate, *i.e.* it is non-stationary. Hence quantum mechanics forces the radical to undergo periodic

stereomutation from R *via* ‡ to P and then from P *via* ‡ back to R, and so on. Since the nuclei of CHFBr dislike the geometry of the transition state, they make it through ‡ as fast as possible, *i.e.* with maximum velocity. The nuclear flux density may be written as nuclear density times a velocity field.[23,32] The very-high tunnelling velocity thus enables the maximum value of the 1D flux density, or the flux, at the potential barrier, in spite of the very low value of the density.

5.4 Application to Electronic Charge Migration in $HCCBr^+$

Let us now switch gears from the rather slow nuclear tunnelling in the typical time domain from picoseconds (ps) to even much longer times,[1] to the ultrafast electronic charge migration in the typical time domain from few hundred attoseconds (as) to few femtoseconds (fs). Our second application of the general quantum theory for the analogy of nuclear tunnelling and electronic charge migration (Section 5.2) is thus to charge migration in the bromo-acetylenic cation, $HCCBr^+$. Again, there are several motivations for the choice of this system.

The $HCCBr^+$ cation is similar to the $HCCI^+$ cation, which serves as a key example. The first joint experimental and theoretical reconstruction and control of charge migration in $HCCI^+$ was demonstrated recently by Wörner with partners and coworkers,[15] see also ref. 14. Here we summarize some important details of their reconstruction in order to set up a model that will then allow us to carry out analogous quantum dynamics simulation of charge migration in $HCCBr^+$. For this purpose, we centre attention on a specific scenario of their experiments, namely, at first, they orient the neutral linear precursor molecule HCCI along an axis that serves as a laboratory fixed z axis, with the C–I bond pointing into the direction $z \geq 0$. By analogy, we shall assume that $HCCBr^+$ is oriented along z, with the origin of the z-coordinate at the C nucleus of the C–Br bond pointing to $z \geq 0$. The generic coordinate "q", which was introduced in Section 5.2, is thus specified as "z", for the present application.

After orientation, an intense laser pulse (maximum intensity closely above 10^{14} W cm^{-2}, wavelength 800 nm, duration about 30 fs, polarization perpendicular to the z-axis) causes tunnel ionization of the neutral precursor, precisely at the selective peak of the laser cycle with maximum electric field strength. The tunnel ionization takes (presumably much) less than 200 as. It prepares the cation in a superposition (5.3) of its electronic ground state (g = $\tilde{X}^+\,^2\Pi$) and the first excited state (e = $\tilde{A}^+\,^2\Pi$). For the example of $HCCI^+$, the corresponding electronic energy gap is $\Delta E = E_e - E_g = 2.23$ eV, at the geometry of the global minimum geometry of the neutral precursor HCCI. Within the next *ca.* 1.7 fs, the electric field changes sign and drives the photo-electron back to the cation. Upon re-collision, the system generates high harmonics that are then used for spectroscopic analysis of the cation.

This allowed the authors of ref. 15 to determine the coefficients in eqn (5.3), with a time resolution of about 100 as. Accordingly, from the perspective of the neutral precursor, the cation is generated with an electron hole centred at the halogen. This can be rationalized because it is easier to photo-detach an electron from a halogen such as iodine or bromine, compared to the hydrogen or carbon atoms of the acetylenic moiety. Changing the perspective from considerations of the electron hole to electrons, the ''reactant'' cation $HCCI^+$ (and, by our assumption, also $HCCBr^+$) is created with some excess electronic charge in the acetylenic moiety.

The authors of ref. 15 checked carefully that the initial state (5.3) is not contaminated by any other states. This provides a two-state (g, e) scenario of charge migration in the cation, along its *z*-axis, perfectly ready for application of the general theory of Section 5.2. The charge migration proceeds in quasi-field-free environment, because the laser field remains perpendicular to the axis of the cation, such that it cannot induce any further electronic transitions. The authors of ref. 15 then carried out quantum dynamics simulations of the charge migration in $HCCI^+$, starting from the initial state (5.3) and using the model of fixed nuclei. They also checked that the populations of the two states do not change due to any other transitions, *i.e.* the charge migration is adiabatic, in accord with the general theory in Section 5.2, *cf.* eqn (5.8). As a result, they discovered the periodic migration of the electron hole, from the initial location at the iodine atom to the acetylenic moiety, and back. In the case of $HCCI^+$, the period of charge migration is $\tau_{chm} = h/\Delta E = 1.85$ fs. The generic notation ''τ'' in Section 5.2 is thus replaced by ''τ_{chm}'' for the present application to charge migration. In the complementary consideration of the excess electronic charge, it flows from its initial preferential localization in the acetylenic moiety [electronic density $\rho_R(z)$ of the ''reactant''] preferably to the halogen atom [electron density $\rho_P(z)$ of the ''product''], and back, during one cycle of charge migration with period τ_{chm}.

As résumé of the key ingredients for the present model of $HCCBr^+$, the authors of ref. 15 reconstructed the charge migration in $HCCI^+$ by means of quantum dynamics simulations, *cf.* eqn (5.8), starting from the initial superposition state (5.3) for the two-state scenario. The nuclei were assumed to be frozen during the period $\tau_{chm} = h/\Delta E = 1.85$ fs, suggesting the model of fixed nuclei.

In addition to the pioneering work of ref. 15, we could reconstruct the flux of the valence electrons along the nuclear axis, during charge migration in $HCCI^+$.[21] For this purpose we employed the same initial state (5.3) and used the same model (two states, fixed nuclei) as in ref. 15. In principle, the total electronic flux should also include the contribution of the core electrons. They travel with the nuclei,[16] however, and since the nuclei are considered to be frozen, the core electrons do not contribute to the electronic flux.

The example of the successful joint experimental and theoretical reconstruction of the electronic charge migration[15] and the electronic flux[21] of the valence electrons in $HCCI^+$ motivates the present analogous quantum dynamics simulation of the charge migration of the valence electrons in

$HCCBr^+$. Accordingly, we employ the two-state model for fixed nuclei. Moreover, we adapt the same methods of *ab initio* quantum chemistry for the calculations of the geometric and energetic properties of $HCCBr^+$ as for $HCCI^+$; for the details, see ref. 33. Specifically, the nuclei of $HCCBr^+$ are frozen in the global minimum geometry of the precursor molecule HCCBr in its ground state $\tilde{X}^+\ ^1\Sigma^+$, as illustrated in Figure 5.2(a). The corresponding lengths of the H–C, C≡C and C–Br bonds are 1.063 Å, 1.208 Å and 1.798 Å, respectively. The electronic Hamiltonian H in the TISE (5.1) consists of the operators of the kinetic energies of all electrons, and the operators for the Coulomb interactions of all electrons and the fixed nuclei. We also investigated the effects of spin–orbit coupling, but they turn out to be negligible for the present purpose.[33]

The TISE (5.1) is solved for the electronic wave functions Ψ_g and Ψ_e and energies E_g and E_e of the electronic ground state ($g = \tilde{X}^+\ ^2\Pi$) and the first excited state ($e = \tilde{A}^+\ ^2\Pi$) at the fixed nuclear geometry. The gap is $\Delta E = E_e - E_g = 2.74$ eV. The related period of charge migration is $\tau_{chm} = h/\Delta E = 1.51$ fs.

The initial state is constructed as superposition (5.3) of Ψ_g and Ψ_e. For the present purpose, *i.e.* for the demonstration of the analogy of nuclear tunnelling and electronic charge migration, we employ the same coefficients $C_g = C_e = 1/\sqrt{2}$ as in Section 5.3, with the same consequences and simplifications, *e.g.* the time shift is equal to zero such that $t' = t$, *etc.*, *cf.* eqn (5.16) and (5.17). As discussed in Section 5.2, this choice yields the most efficient flux; for the present application this means the most efficient charge migration with maximum electronic flux; the present electronic flux in $HCCBr^+$ will, therefore, be more efficient than in the example $HCCI^+$ with the experimentally determined complex and non-equal coefficients, *cf.* ref. 15 and 21. Irrespective of the different coefficients for the initial superposition state (5.3), we still adapt an important property of the example $HCCI^+$, namely, from the perspective of the neutral precursor, it is prepared with electron hole density centred on the halogen, or turning the tables, the excess electron density accumulates in the HCC moiety. Accordingly, we determine the signs of the electronic wave functions Ψ_g and Ψ_e such that the "reactant" and "product" electron densities $\sigma_R(z)$ [eqn (5.18)] and $\sigma_P(z)$ [eqn (5.19)] are prepared with excess valence electron density accumulated in the HCC moiety and at the Br nucleus, respectively; see the discussion after eqn (5.18) and (5.19).

In practice, we first calculate the 3D one-electron densities of the valence electrons in the ground state $[\sigma_g(x, y, z)]$ and the excited state $[\sigma_e(x, y, z)]$ together with the 3D one-electron density difference

$$\Delta\sigma(x, y, z) = -2N_e \int \Pi' dq_{el}\ \Psi_g(q_{el})\ \Psi_e(q_{el}) \tag{5.34}$$

where "$\int \Pi' dq_{el}$" symbolizes the sum over all electron spins and the integral over the spatial coordinates of all electrons but one, and N_e is the number of valence electrons; compare with eqn (5.20) applied to the present case with equal coefficients, eqn (5.22). Subsequently, the 3D one-electron densities of

the valence electrons $\sigma_g(x, y, z)$, $\sigma_e(x, y, z)$ and $\Delta\sigma(x, y, z)$ are integrated over x and y in order to obtain the corresponding 1D axial (z) electron densities of the valence electrons, $\rho_g(z)$, $\rho_e(z)$ and $\Delta\rho(z)$, respectively. The electron yield $y(z)$ can then be calculated according to eqn (5.28),

$$y(z) = -\int_{z_{min}}^{z} dz' \Delta\rho(z') \tag{5.35}$$

with reasonable choice of the lower integration limit ($\Delta\rho(z) \approx 0$ for $z < z_{min}$). The axial electron densities of the "reactant" [*i.e.* the density at ($t = 0$) and the "product" (the density at $t = \tau_{chm}/2$) are then calculated as $\rho_R(z) = \rho_g(z) + \rho_e(z) - \Delta\rho(z)/2$ and $\rho_P(z) = \rho_g(z) + \rho_e(z) + \Delta\rho(z)/2$, compare with eqn (5.18) and (5.19)]. Finally, the time evolution of the electron density $\rho(z, t)$ and the flux $F(z, t)$ are evaluated by the general expressions (5.23), and (5.28) and (5.29) with the substitution $q \rightarrow z$ and $t' = t$.

The resulting axial one-electron densities of the valence electrons $\rho_R(z)$ and $\rho_P(z)$ of the "reactant" and "product" cation $HCCBr^+$ are shown in Figure 5.2(a). They are normalized to the number of valence electrons, $N_e = 1 + 4 + 4 + 7 - 1 = 15$. Apparently, $\rho_R(z)$ and $\rho_P(z)$ have similar overall shapes, with two peaks for the local maxima of the electron densities near to the centre of the C≡C bond and at the Br nucleus. These peaks are separated by local minima of the densities in the C–Br bond. Most important for the present purposes, however, are the differences between $\rho_R(z)$ and $\rho_P(z)$. Apparently, the "reactant" $\rho_R(z)$ accumulates slightly more excess electron density in the acetylenic moiety than the "product" $\rho_P(z)$, whereas the "product" $\rho_P(z)$ is more strongly peaked at the bromine nucleus than the "reactant" $\rho_R(z)$. This preparation of $\rho_R(z)$ and $\rho_P(z)$ in $HCCBr^+$ is consistent with the example $HCCI^+$ for the chosen experimental scenario.[14,15] From this result, one may already anticipate that the dominant flux of the excess electron density in $HCCBr^+$ during the first half period $0 < t < \tau_{chm}/2$ is from the acetylenic moiety to the Br nucleus. This is symbolized by the arrows in the cartoon at the top of Figure 5.2(a).

Figure 5.2(b) shows the difference $\Delta\rho(z) = \rho_P(z) - \rho_R(z)$ of the axial one-electron densities of the "product" minus the "reactant". Essentially, $\Delta\rho(z)$ is negative and positive in the domains of the acetylenic moiety and the Br nucleus, respectively. The corresponding global minima and maxima of $\Delta\rho(z)$ peak at the carbon nucleus of the C–Br bond, and at the Br nucleus, respectively. The switch from dominantly negative to positive values of $\Delta\rho(z)$ occurs in the C–Br bond, near to the local minima of the densities $\rho_P(z)$ and $\rho_R(z)$. In addition, $\Delta\rho(z)$ has several local maxima and minima that are, however, much less pronounced compared to the global extrema. The overall shape of the function $\Delta\rho(z)$ suggests distinguishing the "domains of the reactant and the product" as the domains where $\Delta\rho(z)$ is essentially negative and positive, respectively. The definition of the border z_b between the two domains is somewhat arbitrary, however, due to the small local maxima and minima of $\Delta\rho(z)$. For reference, we set $z_b = 0.50a_0$ – this is the position near to the carbon nucleus of the C–Br bond where $\Delta\rho(z_b) = 0$.

Figure 5.2(b) also has the yield $y(z)$ which is obtained as negative integral of the density difference $\Delta\rho(z)$, *cf.* eqn (3.35). The prominent features of $\Delta\rho(z)$ that are discussed above imply that $y(z)$ is essentially positive, with a plateau type feature in the sub-domain of the C–Br bond which corresponds to the local minima of $\rho_P(z)$ and $\rho_R(z)$ at $z = 1.4a_0$. The global maximum of $y(z)$ is at the border $z = z_b$, which is close to these local minima, but slightly shifted towards the carbon nucleus of the C–Br bond. Close inspection reveals that the yield is negative in the domain well beyond the Br nucleus, albeit with negligibly small absolute values. This is a marginal feature, however, and it is difficult to say whether this is a real phenomenon, or just an artifact due to the fact that the underlying methods of quantum chemistry adapted from ref. 33 are state-of-the-art, but not perfect.

The resulting time evolution of the axial one-electron density $\rho(z, t)$ of the valence electrons of $HCCBr^+$ during the first cycle of charge migration ($0 < t < \tau_{chm} = 1.51$ fs) is shown in Figure 5.4(a). At first glance, the density

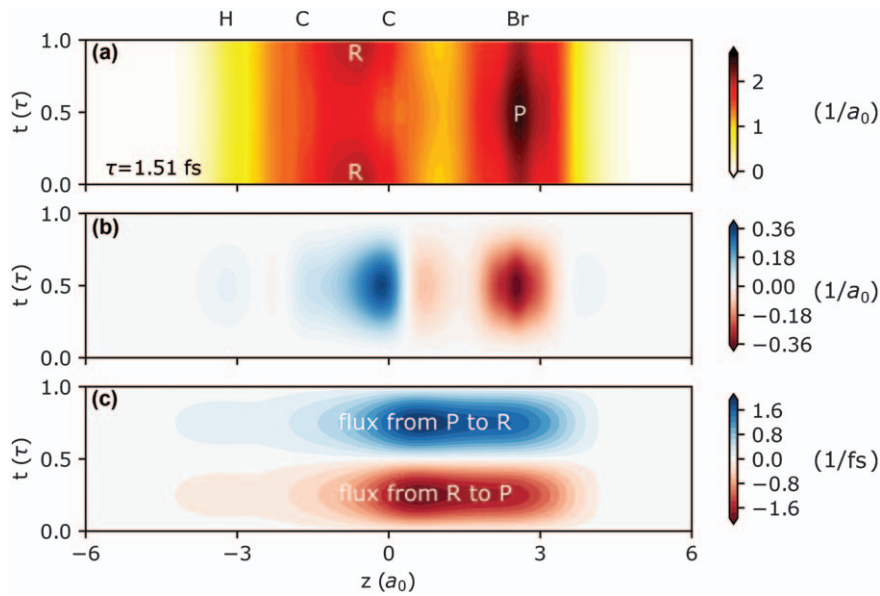

Figure 5.4 Time evolution of the periodic electronic charge migration in the linear $HCCBr^+$ cation along its axis z, during the first period, $0 \le t \le \tau_{chm}$. Initially, the cation is prepared in the "reactant" (R) superposition state $1/\sqrt{2}$ $(\Psi_g + \Psi_e)$ of the electronic ground state Ψ_g ($g = \tilde{X}^+\,^2\Pi$) and the first excited state Ψ_e ($e = \tilde{A}^+\,^2\Pi$). At $t = \tau_{chm}/2$, it arrives at the "product" (P) superposition state $1/\sqrt{2}(\Psi_g - \Psi_e)$ (except for an irrelevant overall phase factor). (a) Time evolution of the one-dimensional (1D) electronic density $\rho(z, t)$ of the valence electrons, from R to P and back to R. (b) Difference in the electronic density $\rho(z, t)$ at time t minus the initial density $\rho(z, 0) = \rho_R(z)$. (c) 1D electronic flux $F(z, t)$, equal to the 1D electronic flux density $j(z, t)$. During the time interval $0 < t < \tau_{chm}/2$ the flux is from R to P. At $t = \tau_{chm}/2$, it changes direction, hence $F(z,\ t = \tau_{chm}/2) = 0$. Subsequently from $\tau_{chm}/2 < t < \tau_{chm}$, the flux is from P back to R. The results (a)–(c) are illustrated by color-coded contour plots.

appears to be rather robust, with two peaks in the C≡C bond and at the Br nucleus, separated by the local minimum in the centre of the C–Br bond. Close inspection reveals, however, that during the first and second half cycles, a relatively small part of the density flows from the initial accumulation in the C≡C bond to the Br nucleus, and back to the C≡C bond, respectively. It is quite remarkable that this apparent shift of what we may call the ''axial excess electron density'' proceeds without any significant changes in the overall density at its local minimum at the centre of the C–Br bond. This effect appears more pronounced in Figure 5.4(b) which shows the difference $\Delta\rho(z, t) = \rho(z, t) - \rho_R(z)$ of the axial one-electron density of the valence electrons at time t minus the initial density $\rho(z, t = 0) = \rho_R(z)$. Obviously, it evolves with temporal symmetry $\Delta\rho(z, t) = \Delta\rho(z, \tau_{chm} - t)$ such that during the first half cycle, the initial axial excess electron density in the C≡C bond is depleted to the benefit of the density at the Br nucleus, and *vice versa* during the second half cycle, without any significant changes $[\Delta\rho(z \approx 1\ a_0, t) \approx 0]$ of the density $\rho(z, t)$ in a wide range around $z = 1.85a_0$ near to its local minimum. Close inspection also reveals a marginal effect of electron depletion and recovery in the domain beyond the Br nucleus, but as for the discussion of $\Delta\rho(z)$ in Figure 5.2(b), it is not clear whether this is a real, albeit very small effect, or an artifact.

Finally, Figure 5.4(c) documents the time evolution of the axial electronic flux $F(z, t)$. Obviously, it proceeds with robust spatial profile given by the yield $y(z)$ shown in Figure 5.2(b), modulated by the periodic sinusoidal function, with corresponding temporal symmetry $F(z, t) = F(z, \tau_{chm}/2 - t) = -F(z, \tau_{chm}/2 + t) = -F(z, \tau_{chm} - t)$. Accordingly, during the first and second half cycles, the dominant flux of the excess electron density is from the acetylenic moiety *via* the sub-domain of the C–Br bond with minimum density to the Br nucleus, and back, with maximum absolute values $\max|F(z, t)|$ at $z = z_b$ for $t = \tau_{chm}/4$, $3\tau_{chm}/4$, $5\tau_{chm}/4$, $7\tau_{chm}/4$, *etc.* There are also marginal fluxes in opposite directions, in the domain beyond the Br nucleus, [hardly visible on the colour code scale of Figure 5.4(c)], but, as discussed before, it is not clear whether these are real, albeit negligible effects, or artifacts.

5.5 Comparison of the Results for Stereomutation of CHFBr by Nuclear Tunnelling and for Axial Electronic Charge Migration in $HCCBr^+$

In this section, we compare the results derived in Sections 5.3 and 5.4 for stereomutation of CHFBr by nuclear tunnelling and for axial electronic charge migration in $HCCBr^+$. For this purpose, we inspect the corresponding analogous panels (a), (b), *etc.* of Figures 5.1 and 5.3, and 5.2 and 5.4, respectively, keeping in mind the underlying theory presented in Section 5.2.

As anticipated in the introduction, Figures 5.1(a) and 5.2(a) are entirely different, because they have the cartoons of the nuclear and electronic processes and the corresponding densities of the ''reactants'' and

"products" that are so entirely different. The nuclear and electronic energy gaps ΔE between the levels of the ground and excited nuclear and electronic states that are involved in the processes differ by more than three orders of magnitude. As a consequence, the resulting periods $\tau = h/\Delta E$ also differ by more than three orders of magnitude.

In spite of the enormous qualitative and quantitative differences between the systems and processes illustrated in Figures 5.1(a) and 5.2(a), the rest of the figures reveal impressive analogies. These will be detailed below. For this purpose, we switch back to the generic notation used in Section 5.2, *i.e.* we use the period "τ" and the coordinate "q", instead of the individual "τ_{stereo}" or "τ_{chm}" and "α_{u}" or "z", respectively. The notation "q_{b}" means the border between the domains of the reactant (R, $q < q_{\mathrm{b}}$) and the product (P, $q > q_{\mathrm{b}}$), corresponding to the domains "$\alpha_{\mathrm{u}} < 0$" or "$z < z_{\mathrm{b}}$" and "$\alpha_{\mathrm{u}} > 0$" or "$z > z_{\mathrm{b}}$", respectively. When we talk about the "densities" or the "fluxes" (plural!) below, we always mean the corresponding quantities for the two processes: nuclear tunnelling and electronic charge migration.

Close inspection of the remaining Figures 5.1(b) and 5.3 for nuclear tunnelling (Section 5.3) and 5.2(b) and 5.4 for electronic charge migration (Section 5.4) reveals the equivalence of the following phenomena for the two applications.

(i) The density differences $\Delta\rho(q) = \rho_{\mathrm{P}}(q) - \rho_{\mathrm{R}}(q)$ of the reactant (R) and the product (P) are essentially negative in the domain of R, but positive for P, *cf.* Figures 5.1(a) and 5.2(a). The word "essentially" here emphasizes the most prominent properties and disregards the marginal deviations discussed in Section 5.4, and which are actually so small that it is hard to say whether they are real, albeit with entirely negligible effects, or just artifacts.

(ii) The yields $y(q)$ have their maxima at the border q_{b} between the domains of the reactant and the product. Moreover, the yields have plateaus near to their maxima, *cf.* Figures 5.1(a) and 5.2(a).

(iii) The time evolutions of the densities $\rho(q, t)$ and of the fluxes $F(q, t)$ are periodic, with period τ, *cf.* Figures 5.3 and 5.4.

(iv) The time evolutions of the differences $\Delta\rho(q, t) = \rho(q, t) - \rho(q, t = 0)$ of the densities at time t minus the initial densities $\rho(q, t = 0) = \rho_{\mathrm{R}}(q)$ have temporal symmetries, $\Delta\rho(q, t) = \Delta\rho(q, \tau - t)$, *cf.* Figures 5.3(b) and 5.4(b).

(v) Likewise, there are temporal symmetries for the fluxes, $F(q, t) = F(q, \tau/2 - t) = -F(q, \tau/2 + t) = -F(q, \tau - t)$, *cf.* Figures 5.3(c) and 5.4(c).

(vi) The density differences $\Delta\rho(q, t)$ are essentially negative in the reactant domains but positive in the product domains. The values of $\Delta\rho(q, t)$ are negligible for values of q close to the borders q_{b} between the two domains, *cf.* Figures 5.3(b) and 5.4(b). This means that during the full cycles ($0 < t < \tau$), the densities, or part of them, are shifted from R to P, and then back to R, without any significant changes in the densities at the border between R and P. This result

for the density differences $\Delta\rho(q, t)$ is of course confirmed by the time evolutions of the densities, *cf.* Figures 5.3(a) and 5.4(a).

(vii) The fluxes $F(q, t)$ are essentially positive, *i.e.* from R along q to P during the first half cycles $(0 < t < \tau/2)$ but negative, *i.e.* from P back to R during the second half cycles $(\tau/2 < t < \tau)$. They vanish for $t = 0$, $\tau/2$, τ, *etc.* with periodic continuations. At all other times $(t \neq 0, \tau/2, \tau, \textit{etc.})$, $F(q, t)$ has extreme values at the borders q_b between the reactant and product domains. The absolute maxima and minima of the fluxes are obtained at the borders q_b at times $t = \tau/4$, $3\tau/4$, and then with periodic continuations at $5\tau/4$, $7\tau/4$, *etc.*, *cf.* Figures 5.3(c) and 5.4(c).

(viii) The fluxes $F(q, t)$ have plateaus in the vicinities of their maxima or minima, *cf.* Figures 5.3(c) and 5.4(c).

In brief, all phenomena (i)–(viii) imply that the densities, or part of the densities, are shifted periodically from R to P and then back from P to R, during one cycle with period τ. The processes proceed such that during the first half cycle, P grows at the expense of R, and *vice versa* during the second half cycle, without any significant variations of the densities at the borders q_b between the reactant and product domains. This is achieved by fluxes with plateau-type shapes and maximum or minimum values half-way between R and P, or between P and R.

The similarity of the phenomena (i)–(viii) reveal and document the analogy of the two processes, nuclear tunnelling and electronic charge migration, at least for the quite realistic two-state scenarios we employed in Sections 5.2–5.4.

5.6 Conclusions

We have evaluated the time evolutions of the densities and the fluxes of two different processes of two entirely different model systems and discovered close analogies in the quantum dynamics. The first case study is for periodic stereomutation from the oriented non-linear (*S*)-CHFBr to (*R*)-CHFBr and back to (*S*)-CHFBr by coherent nuclear tunnelling, with period $\tau_{stereo} = 10.57$ ps. Here (at least one of) the nuclei move with rather large amplitudes, and the electrons remain in the electronic ground state. The second case is periodic electronic charge migration in the oriented linear $HCCBr^+$ cation, with much shorter period $\tau_{chm} = 1.51$ fs. On this time scale, the nuclei are essentially frozen, and the electrons evolve coherently in the electronic-ground and first-excited states. The analogies of the quantum dynamics are documented in Figures 5.1(b) and 5.3 for nuclear tunnelling, and in Figures 5.2(b) and 5.4 for electronic charge migration, respectively, and they are listed as eight common features (i)–(viii) in Section 5.5.

In the context of this book,[3] we would like to conclude by extending a working hypothesis,[24] namely, the analogies of the quantum dynamics of nuclear tunnelling and electronic charge migration suggest that, not only the stereomutation of CHFBr but also the charge migration in oriented

$HCCBr^+$, share common features of tunnelling. To support this hypothesis, let us first recall (at least) three kinds of quantum mechanical nuclear tunnelling that are documented in the literature. The first and ''standard'' type of tunnelling is ''tunnelling through a potential barrier $V^{\ddagger}$'', or briefly ''potential tunnelling''.[1–3] Here the barrier $V^{\ddagger}$ separates two domains of the molecular system that may be referred to as the domains of the ''reactant'' (*R*) and of the ''product'' (P). The total energy of the system is below the barrier, $E < V^{\ddagger}$. As a consequence, transitions from R to P or from P to R are classically forbidden. Nevertheless, they are allowed by quantum mechanics – ''potential tunnelling'' is a quantum effect. No doubt, the stereomutation of CHFBr proceeds by potential tunnelling.

The second type of tunnelling is ''dynamical tunnelling'', discovered by Davis and Heller.[34] As in the case of potential tunnelling, dynamical tunnelling is a quantum effect that enables the transition between two molecular domains even though it is classically forbidden. In this case, however, the classical constraint is quite different from the traditional constraint $E < V^{\ddagger}$, namely, it is a ''dynamical constraint.'' It may arise at higher energies $E > V^{\ddagger}$, and in fact, it may arise even in systems that do not possess any potential barrier at all. In a classical picture, for example, the system may be prepared with specific initial conditions such that it evolves along one of two separate stable periodic orbits that co-exist at the same total energy *E*. As the name suggests, these orbits are periodic, which means that, in the frame of classical mechanics, the system must stay on its orbit; it must not ''hop'' to the other periodic orbit. The word ''stable periodic orbit'' indicates that if one prepares the system in a sufficiently near neighbourhood of the periodic orbit, *e.g.* in a narrow torus about the orbit, it still cannot ''hop'' into the corresponding torus about the other orbit. In quantum mechanics, the tori about the two different classical periodic orbits correspond to two different wave functions that extend along the orbits. Davis and Heller have shown that if one prepares the molecular system in a wave function that corresponds to one of two separate classical orbits, then it can make a transition to the other wave function that extends along the other orbit, even though this is classically forbidden. This process is called ''dynamical tunnelling''.[34]

The third kind of tunnelling was discovered by Hashimoto and Takatsuka[35] for systems that possess two separate instable periodic orbits, at the same total energy, in the frame of classical mechanics. The word ''instable'' indicates that if one prepares the system with initial conditions close to one of the periodic orbits, then it may hop to the neighbourhood of the other orbit. The time evolution of this type of transition has some important characteristic features. Namely, at first, the system cycles close to the initial periodic orbit. Next, after (very!) many such cycles, it makes a sudden hop to the vicinity of the other periodic orbit. Then it continues to cycle about the other periodic orbit, again for many times. This temporal pattern reminds us of the properties of potential tunnelling discussed above, *i.e.* the systems prefer to stay in the domains of R and P for rather long times until they make a sudden transition from R to P, or *vice versa.*[23] Hashimoto and Takatsuka

have shown that quantum mechanically, if one prepares the system in the corresponding initial wave function that extends along one of the instable periodic orbits, then its density decreases to the benefit of the density close to the other orbit. This transition occurs without any significant appearance of density in the domains between the two orbits.

The quantum dynamics of the present charge migration in $HCCBr^+$ proceeds in a way that reminds us of the type of dynamical tunnelling discovered by Hashimoto and Takatsuka.[35] For example, the time evolution of the electronic density difference documented in Figure 5.4 is analogous to the time evolution of the nuclear density during dynamical tunnelling, as documented in figure 7 of ref. 35. This leads to our working hypothesis: charge migration in oriented $HCCBr^+$ can be described as dynamical tunnelling. Of course, there are also important differences. Most important: Hashimoto and Takatsuka describe nuclear dynamical tunnelling,[35] whereas the present charge migration would correspond to electronic dynamical tunnelling.

Our working hypothesis is also supported by a re-consideration or re-interpretation of the strikingly different time scales, $\tau_{stereo} = 10.57$ ps *versus* $\tau_{chm} = 1.51$ fs. The rather long period τ_{stereo} is for nuclear potential tunnelling. It is well known that the corresponding times for electronic potential tunnelling are much shorter. For example, the preparation of the initial superposition state (5.3) by photo-ionization of the neutral precursor proceeds by electronic potential tunnelling in the time domain below 100 as.[14,15] Likewise, nuclear dynamical tunnelling as discovered by Hashimoto and Takatsuka is a rather slow process in the ps or even much longer time domain. By analogy, electronic dynamical tunnelling should take much shorter times, actually in the sub-fs time domain for the transition in one direction, $\tau_{chm}/2 = 750$ as.

The present analogy has been discovered for rather simple model systems: they are oriented, they are prepared initially as a superposition of two eigenstates (the ground state and the first-excited states), the quantum dynamics evolve adiabatically, *i.e.* without any transitions between the two states or any others, and they are essentially along one degree of freedom (DOF), without any considerations of the effects of other DOFs that cause decoherence,[36–40] see also ref. 33. It is a challenge to investigate whether the analogy of nuclear tunnelling and electronic charge migration persists in more demanding systems, *i.e.* in molecules that are prepared in a superposition of more than two states, or with diabatic transitions, or with additional significant DOFs, or with competing effects of decoherence.

Acknowledgements

One of us (VS) expresses deep gratitude to his thesis supervisor, Professor H. J. Wörner (ETH Zürich) for stimulating guidance and advice. We also thank Professor K. Takatsuka (The University of Kyoto) for valuable guidance to part of the literature. Generous financial support by the National Key Research Program of China (no. 2017YFA0304203), the program for

Changjiang Scholars and Innovative Research Team (no IRT_17R70), the hundred talent program of Shanxi province, the 111 project (Grant D18001) and the Fund for Shanxi ''1331 Project Key Subjects'' is also gratefully acknowledged. AS is grateful for financial support by an Ambizione grant of the Swiss National Science Foundation.

References

1. F. Hund, *Z. Phys.*, 1927, **43**, 805.
2. C. Fábri, R. Marquardt, A. G. Császár and M. Quack, *J. Chem. Phys.*, 2019, **150**, 014102.
3. S. Kozuch and J. Kästner, *Tunnelling in Molecules – Nuclear Quantum Effects from Bio-to Physical Chemistry*, The Royal Society of Chemistry, London, 2020.
4. H. Eyring, J. Walter and G. E. Kimball, *Quantum Chemistry*, Wiley, New York, ch. 11, 1944.
5. D. J. Diestler, G. Hermann and J. Manz, *J. Phys. Chem. A*, 2017, **121**, 5332.
6. R. Weinkauf, P. Schanen, A. Metsala, E. W. Schlag, M. Bürgle and H. Kessler, *J. Phys. Chem.*, 1996, **100**, 18567.
7. L. S. Cederbaum and J. Zobeley, *Chem. Phys. Lett.*, 1999, **307**, 205.
8. G. L. Yudin, S. Chelkowski, J. Itatani, A. D. Bandrauk and P. B. Corkum, *Phys. Rev. A*, 2005, **72**, 051401.
9. F. Remacle and R. D. Levine, *Proc. Natl. Acad. Sci. U. S. A.*, 2006, **103**, 6793.
10. I. Barth and J. Manz, *Angew. Chem., Int. Ed.*, 2006, **45**, 2962.
11. M. Kanno, H. Kono and Y. Fujimura, *Angew. Chem., Int. Ed.*, 2006, **45**, 7995.
12. S. Chelkowski, G. L. Yudin and A. D. Bandrauk, *J. Phys. B: At., Mol. Opt. Phys.*, 2006, **39**, S409.
13. D. Jia, J. Manz, B. Paulus, V. Pohl, J. C. Tremblay and Y. Yang, *Chem. Phys.*, 2017, **482**, 146.
14. H. J. Wörner, C. A. Arrell, N. Banerji, A. Cannizzo, M. Chergui, A. K. Das, P. Hamm, U. Keller, P. M. Kraus, E. Liberatore, P. Lopez-Tarifa, M. Lucchini, M. Meuwly, C. Milne, J.-E. Moser, U. Rothlisberger, G. Smolentsev, J. Teuscher, J. A. van Bokhoven and O. Wenger, *Struct. Dyn.*, 2017, **4**, 061508.
15. P. M. Kraus, B. Mignolet, D. Baykusheva, A. Rupenyan, L. Horný, E. F. Penka, G. Grassi, O. I. Tolstikhin, J. Schneider, F. Jensen, L. B. Madsen, A. D. Bandrauk, F. Remacle and H. J. Wörner, *Science*, 2015, **350**, 790.
16. T. Bredtmann, D. J. Diestler, S.-D. Li, J. Manz, J. F. Pérez-Torres, W.-J. Tian, Y.-B. Wu, Y. Yang and H.-J. Zhai, *Phys. Chem. Chem. Phys.*, 2015, **17**, 29421.
17. Vít Svoboda, Niraghatam Bhargava Ram, Denitsa Baykusheva, Daniel Zindel, Benjamin Spenger, Manuel Ochsner, Holger Herburger, Jürgen

Stohner, and Hans Jakob Wörner, Femtosecond photoelectron circular dichroism of chemical reactions, Science Advances, submitted, 2020.
18. V. Svoboda, Ph.D. Thesis, ETH Zürich, 2019.
19. M. Born and R. Oppenheimer, *Ann. Phys.(Leipzig)*, 1927, **84**, 457.
20. M. Born and K. Huang, *Dynamical Theory of Crystal Lattices*, Oxford University Press, London, Appendix VIII, 1954, p. 406.
21. H. Ding, D. Jia, J. Manz and Y. Yang, *Mol. Phys.*, 2017, **115**, 1813.
22. J. Manz and K. Yamamoto, *Mol. Phys.*, 2012, **110**, 517.
23. T. Grohmann, J. Manz and A. Schild, *Mol. Phys.*, 2013, **111**, 2251.
24. G. Hermann, C. Liu, J. Manz, B. Paulus, J. F. Pérez-Torres, V. Pohl and J. C. Tremblay, *J. Phys. Chem. A*, 2016, **120**, 5360.
25. C. Liu, J. Manz and Y. Yang, *Phys. Chem. Chem. Phys.*, 2016, **18**, 5048.
26. J. R. Letelier and C. A. Utreras-Días, *Spectrochim. Acta, Part A*, 1997, **53**, 247.
27. R. Meyer and H. H. Günthard, *J. Chem. Phys.*, 1968, **49**, 1510.
28. F. Neese, The ORCA program system, *Wiley Interdiscip. Rev.: Comput. Mol. Sci.*, 2011, **2**, 73.
29. J. M. L. Martin and A. Sundermann, J. Chem. Phys., 2001, **114**, 3408.
30. D. T. Colbert and W. H. Miller, *J. Chem. Phys.*, 1992, **96**, 1982.
31. J. Manz, A. Schild, B. Schmidt and Y. Yang, *Chem. Phys.*, 2014, **442**, 9.
32. M. V. Berry, *Eur. J. Phys.*, 2013, **34**, 1337.
33. D. Jia, J. Manz and Y. Yang, *J. Phys. Chem. Lett.*, 2019, **10**, 4273.
34. M. J. Davis and E. J. Heller, *J. Chem. Phys.*, 1981, **75**, 246.
35. N. Hashimoto and K. Takatsuka, *J. Chem. Phys.*, 1998, **108**, 1893.
36. A. D. Bandrauk, S. Chelkowski, P. B. Corkum, J. Manz and G. L. Yudin, *J. Phys. B: At., Mol. Opt. Phys.*, 2009, **42**, 134001.
37. H. Mineo, S. H. Lin and Y. Fujimura, *Chem. Phys.*, 2014, **442**, 103.
38. C. Arnold, O. Vendrell and R. Santra, *Phys. Rev. A*, 2017, **95**, 033425.
39. M. Vacher, M. J. Bearpark, M. A. Robb and J. P. Malhado, *Phys. Rev. Lett.*, 2017, **118**, 083001.
40. V. Depré, N. V. Golubev and A. I. Kuleff, *Phys. Rev. Lett.*, 2018, **121**, 203002.